Computers and Geotechnics 197 (2026) 108230

Contents lists available at ScienceDirect

Computers and Geotechnics

journal homepage: www.elsevier.com/locate/compgeo

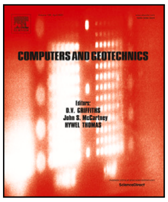

Research paper

Discrete element modeling of non-uniform biocementation in sand

Huanran Wu [a,b,c], Yang Xiao [a,b,c,*], Weijian Liang [d], Jidong Zhao [e], T. Matthew Evans [f]

[a] *School of Civil Engineering, Chongqing University, Chongqing, 400045, China*
[b] *State Key Laboratory of Safety and Resilience of Civil Engineering in Mountain Area, Chongqing, 400045, China*
[c] *Innovation Center for Biogenic Construction Technology, Chongqing University, Chongqing, 400045, China*
[d] *College of Civil and Transportation Engineering, Shenzhen University, Shenzhen, 518060, China*
[e] *Department of Civil and Environmental Engineering, Hong Kong University of Science and Technology, Clearwater Bay, Kowloon, Hong Kong, China*
[f] *School of Civil and Construction Engineering, Oregon State University, Corvallis, OR 97331, United States*

ARTICLE INFO

Keywords:
Biocementation
Non-uniform
Compressive strength
Discrete element modeling
Failure

ABSTRACT

The non-uniform distribution of $CaCO_3$ crystals is a ubiquitous phenomenon in biocementation, and is recognized as a critical factor influencing its mechanical performances. However, the non-uniform biocementation has not been thoroughly investigated due to challenges in quantitatively controlling the uniformity in experiments. In this study, we employ a 3D Discrete Element Method (DEM) approach to model non-uniform biocementation, using cementing fines to represent the $CaCO_3$ crystals. We generate two typical distribution patterns often encountered in element-scale biocemented specimens at varying degrees of non-uniformity to assess their effects on mechanical responses. The uniform specimen exhibits the best performance, followed by those with a cemented hull. Specimens with axial non-uniformity show the greatest sensitivity to the degree of non-uniformity and the poorest mechanical performance. Failure in the specimens with axial non-uniformity tends to localize in the weakly-cemented layers, while the uniform specimen and those with a cemented hull typically develop clear shear bands that cut through the specimens. Additionally, the evolution of the force chain network and contact-based anisotropy further emphasizes the role of weakly-cemented regions in the failure process. This study quantitatively examines the influences of non-uniform biocementation and provides valuable insights for element-scale experiments and practical applications of biocementation techniques.

1. Introduction

Applying biological materials and processes to conventional engineering activities has become a rising trend, considering the great potential of biological systems for engineering solutions (Mitchell and Santamarina, 2005; Dejong et al., 2013). Microbially induced carbonate precipitation (MICP) has attracted much interest as a green geotechnical reinforcement technique, holding the potential to reduce CO_2 emissions relative to conventional Portland cement-based techniques (DeJong et al., 2010; Okyay et al., 2016). The MICP process has been investigated substantially from different perspectives, as a soil improvement technique for the bioclogging and biocementation effects (Ivanov and Chu, 2008). The mechanisms of biomineralization, e.g., the formation and the evolution of the $CaCO_3$ crystals, and the microscopic interactions between the bacteria and the biochemical environments, have been investigated through microfluidic chip experiments (Wang et al., 2019; Xiao et al., 2021a; Zhao et al., 2023). The interparticle compressive, tensile, and shear characteristics of biocementation bonds have been investigated through particle-scale mechanical loading tests (Feng, 2015; Ham et al., 2022; Gao et al., 2023; Xiao et al., 2023, 2024b, 2026; Sarkis et al., 2024, 2025). Element-scale experiments have been conducted extensively to examine the capability of various MICP techniques for improving the physical and mechanical characteristics (Montoya et al., 2013; Montoya and DeJong, 2015; Feng and Montoya, 2016; Cui et al., 2024; Ahenkorah et al., 2024; Xiao et al., 2021c, 2024a, 2022a). Furthermore, physical model tests and pilot tests in the field have been reported to evaluate the applicability and performance of MICP at larger scales (van Paassen et al., 2010; Ghasemi and Montoya, 2022; Xiao et al., 2022b; Wang et al., 2024; Liu et al., 2025).

Among all these tests, MICP can generally improve the mechanical properties of soils by forming interparticle bonds among sand particles. Unlike conventional soil improvement techniques involving inorganic matter only, the MICP process involves living bacteria and makes the entire process much more complex (Dejong et al., 2013). Taking the unconfined compressive strength (UCS), the mostly adopted mechanical property, as an example, a great dispersion has been noted under

---

[*] Corresponding author at: School of Civil Engineering, Chongqing University, Chongqing, 400045, China.
E-mail address: xiaoy@cqu.edu.cn (Y. Xiao).

https://doi.org/10.1016/j.compgeo.2026.108230
Received 12 October 2025; Received in revised form 27 March 2026; Accepted 7 May 2026

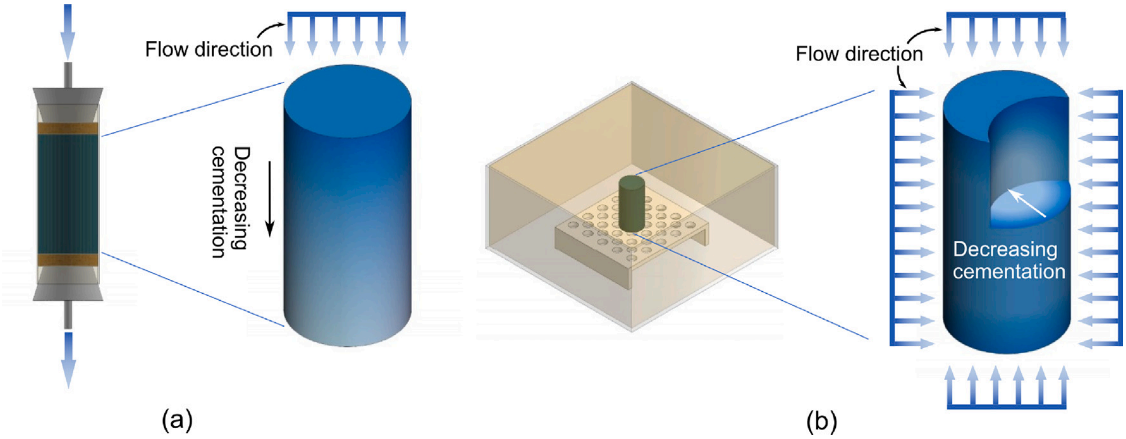

Fig. 1. Illustration of the two typical MICP schemes and the corresponding non-uniform patterns in the laboratory: (a) the biogrouting scheme and the specimen with axial non-uniformity, and (b) the immersing scheme and the specimen with a cemented hull.

the same global $CaCO_3$ content (C_c) even for the same type of sand, despite the general positive correlation between C_c and UCS reported by various researchers (Choi et al., 2020; Mori and Uday, 2022; Sang et al., 2023). From the point of view of the biocemented specimens, the fluctuations in mechanical responses might be caused by the variation in the properties of the sand matrix, e.g., the relative density, particle size, particle shape, etc. (Nafisi et al., 2020; Fu and Haigh, 2024; Liufu et al., 2023; Konstantinou et al., 2023), and the cementation properties, e.g., the spatial distribution, precipitation pattern, and morphological characteristics of the $CaCO_3$ crystals (Cui et al., 2024; Mori and Uday, 2022; Zhang and Dieudonné, 2023; Wang et al., 2023). Specifically, the non-uniform spatial distribution of $CaCO_3$ has been recognized as a critical issue in MICP, hindering the extensive practical applications of this technique (van Paassen et al., 2010). Biogrouting, as the most popular MICP scheme which grouts the bacterial and cementation solutions into the pore space of the geotechnical material under gravity or pressure, would generally induce a preference for precipitation near the inlet and a reduction in local $CaCO_3$ content (C_l) along the increasing length of the percolation path, as illustrated in Fig. 1(a) (Whiffin et al., 2007; Zheng et al., 2023). With the significance of uniformity in mind, several modified biogrouting schemes have been proposed, e.g., the temperature-controlled one-phase scheme (Xiao et al., 2021b), the low-pH one-phase scheme (Cheng et al., 2019; Cui et al., 2021; Lai et al., 2023), and the one-phase scheme with inhibitor (Zhu et al., 2025), trying to improve the uniformity of $CaCO_3$ precipitation. Besides the biogrouting scheme, another common MICP scheme would be immersing the pre-treatment specimen into the cementation solution and allowing the effective materials to permeate into the specimen, as illustrated in Fig. 1(b) (Zhao et al., 2014a; Li et al., 2023), in which a hull with higher cementation has been reported (Zhao et al., 2014b). The distribution of C_l along the percolation direction is often evaluated quantitatively to analyze the uniformity of the specimen, and it is generally concluded that a more uniform distribution of $CaCO_3$ would lead to a better mechanical performance. However, an a posteriori method of analysis is often conducted in these studies, without detailed analysis of the role of uniformity, given the difficulties in controlling a priori the degree of non-uniformity in practical experiments.

In contrast to the inevitable dispersion of results in practical experiments, discrete element method (DEM) modeling has been widely adopted to quantitatively investigate the microscopic characteristics of cemented granular materials under well-controlled initial and boundary conditions (Shen et al., 2016; Wu et al., 2018b, 2020a). Specifically, the DEM modeling has been adopted to explore the micromechanical responses of biocemented sand from various perspectives. The classical scheme modeling the interparticle cementation with well-established parallel bonds can capture the strength improvement efficiently (Feng et al., 2017) and account for the particle-scale variations in biocementation (Zhao et al., 2025), while underestimates the post-peak strength due to the lack of the densification effect from the degraded cementation. The cohesive contact model with moment resistance, a simple and efficient bond model, has been adopted to capture real contact properties based on high-fidelity X-ray microtomography images considering the effects of the cohesive contact surface area distribution and the percentage of cemented contacts (Sarkis et al., 2022) and to consider the solid-fluid interactions (Yang et al., 2025). Moreover, the precipitation patterns of $CaCO_3$, the crystal features and their mechanical effects have been analyzed with cementing fines representing the $CaCO_3$ crystals (Evans et al., 2015; Wu et al., 2023; Zhang and Dieudonné, 2023; Gong et al., 2023). Inspired by this scheme, specimens of various non-uniform patterns and degrees of non-uniformity can be prepared readily by introducing non-uniformly distributed cementing fines, and the role of non-uniform biocementation could be directly analyzed with DEM modeling in an a priori manner. In this study, biocemented sand specimens with two typical non-uniform patterns are prepared, i.e., the specimens with axial non-uniformity and the specimens with a cemented hull. The global mechanical responses, the failure process, and the failure pattern are analyzed, along with the microscopic characteristics, including the interparticle contact force and the contact-based anisotropy. This study specifically focuses on the quantitative effects of non-uniform biocementation on the mechanical responses and will provide valuable reference to the element-scale experiments and inspirations for practical applications of biocementation techniques.

2. Methodology

In this study, we employ a novel DEM scheme with physical entities representing $CaCO_3$ crystals to generate specimens with various non-uniform distributions of $CaCO_3$ crystals and investigate quantitatively the influences of non-uniform biocementation on mechanical responses. The key features of this scheme are introduced herein for completeness. Refer to Wu et al. (2023) for more details of the DEM scheme.

2.1. Numerical biocementing scheme

The DEM scheme is characterized by a numerical biocementing process with fines as cementing agents, mimicking the MICP process in practical experiments. The pre-treatment sand specimen is prepared by settling a random cloud of sand particles under gravity into a cylindrical mold consisting of 64 vertical walls and a bottom plate. A top plate with 10 kPa vertical stress is introduced after the settlement of the sand particles, and the gravity is removed to produce a uniform distribution of the sand particles. Then, cementing fines are inserted randomly into the pore space of the well-prepared pre-treatment specimen, representing the $CaCO_3$ crystals in reality. The size of the fines is determined based on SEM observations, which also ensures that the fines can pass through the pore throats among sand particles. The specimen is divided into several sections, and the number of fines in each section is calculated based on C_l to generate non-uniform biocementation. After that, driving forces along random directions are assigned to the cementing fines and settle them down to local stable positions, where the driving forces are balanced by interparticle cohesion and the normal and shear forces. The driving force on each cementing fines is determined following:

$$\mathbf{F}_i = F_d m_i \mathbf{n}_d \tag{1}$$

where F_d is a microstructural factor controlling the magnitude of the force, m_i is the mass of the fines particle, and $\mathbf{n}_d$ is a unit vector following a random spherical distribution. A higher F_d would lead to a larger driving force during the numerical biocementing process, which can hardly be balanced by the cohesion and friction from a single sand particle, leading to a more effective microstructure and better mechanical responses (Wu et al., 2023). A specific value of 2.7 m/s^2 is adopted in this study after careful model calibration based on experimental results on MICP-treated glass beads in (Xiao et al., 2019). After the stabilization of the fines, interparticle bonds are assigned at the coarse-fine contacts and the fine-fine contacts to generate a stable biocemented specimen. The vertical walls of the mold can be removed thereafter, and the specimen is ready for loading.

Notably, the contacts between the sand particles are pure frictional, while those involving fines are cohesive initially with interparticle bonds and purely frictional upon bond breakage. The purely frictional contact is simply governed by a linear force–displacement law and a Coulomb-type friction. The normal stiffness and the shear stiffness are determined as:

$$k_n = \frac{k_1 k_2}{k_1 + k_2} \tag{2}$$

$$k_s = \nu k_n \tag{3}$$

where $k_i = 2E_i r_i$, with $i = 1, 2$, are the normal contact stiffness of the particles; r_i are the radii of the particles; E and ν are two stiffness parameters. Then, the normal and shear force are calculated as:

$$\mathbf{F}_n = -k_n u_n \mathbf{n}_n \tag{4}$$

$$\mathbf{F}_s = -\min(k_s u_s, F_n \tan(\phi))\mathbf{n}_s \tag{5}$$

where u_n and u_s are the relative normal and shear displacement, respectively; $\mathbf{n}_n$ and $\mathbf{n}_s$ are the unit normal and shear vector of the contact, respectively; ϕ is the interparticle friction angle. The bond strength is characterized by a maximum tensile force and a maximum shear force:

$$F_n^{\max} = c\min(r_1, r_2)^2 \tag{6}$$

$$F_s^{\max} = c\min(r_1, r_2)^2 + F_n \tan(\phi) \tag{7}$$

where c is the bond strength parameter which is assumed to be the same for tensile and shear forces for simplicity; and $F_n \tan(\phi)$ represents the Coulomb-type frictional shear force limit. With consideration of the physical cementing agents and the reproduction of the complex particle-scale microstructure, the bonded contact model is adequate to capture the mechanical responses of interest after a careful model calibration without an explicit consideration of moments.

2.2. Model set-up for uniaxial compressive tests

Uniaxial compression tests are conducted on the prepared biocemented specimens with loading plates at the top and the bottom of the specimen. The prototype of the simulation is uniaxial compression experiments on biocemented spherical glass beads with three levels of cementation (C_c = 6.0%, 10.4%, 13.5%) (Xiao et al., 2019), chosen specifically to avoid the shape effect of the sand particles. The height-to-diameter ratio of the specimen is 2:1, the same as that of the physical specimen. The radii of the sand particles are scaled up by 600 times to speed up the simulation, while maintaining a uniform distribution based on the monosized glass beads of 0.1–0.15 mm in radius. The pre-treatment specimen consists of around 2300 sand particles, which is determined based on parametric analyses with less than 5% fluctuations among parallel realizations. The specimen has an initial porosity of 0.406, corresponding to a relative density of 40%. Notably, a typical biocemented specimen of moderate cementation level (C_c = 10.4%) has around 40,000 fines. The internal friction angle between the plates and the particles is 11.3° with a friction coefficient of 0.2. A nominal axial strain rate of 5×10^{-3} s^{-1} is adopted to guarantee the quasi-static loading condition. The microscopic parameters of the model are calibrated based on the experimental data, e.g., the parameters governing the stiffness (E and ν), the bond strength (c), and the microstructure (F_d). The calibrated model parameters for the DEM particles, listed in Table 1, are capable of reaching a good agreement between the numerical and the experimental results for various levels of uniform biocementation (Wu et al., 2023).

Table 1
Microscopic parameters for the sand and $CaCO_3$ particles.

Material	Particle density (kg/m^3)	r (mm)	E (MPa)	ν	ϕ (°)	c (MPa)
Sand grain	2350	60–90	13.0	0.6	26.6	/
$CaCO_3$ crystal	2710	11.54	84.5	0.6	26.6	3.7

2.3. Specimens with non-uniform biocementation

In physical experiments, the uniformity of the biocementation is often evaluated with the distribution of local $CaCO_3$ content (C_l) within the specimen (Xiao et al., 2021b; Cheng et al., 2019). With physical entities representing the $CaCO_3$ crystals in the soil matrix, numerical avatars of the biocemented sand specimens with various non-uniform patterns and degrees of non-uniformity could be reproduced directly as designed with the DEM scheme. In contrast to the complex experimental conditions leading to possible inconsistent outcomes, those influencing factors besides the well-designed non-uniform biocementation could be well-controlled, which makes it possible to evaluate the role of uniformity precisely. Specifically, specimens with a moderate level of cementation (C_c = 10.4%) are adopted herein, allowing the possible fluctuations in C_l for different regions in the specimen.

A typical non-uniform pattern in element-scale specimens is the axial non-uniformity which occurs during the biogrouting into cylindrical specimens along the axial direction as shown in Fig. 1(a). It has been widely reported that C_l may vary along the axial direction in this case, presenting higher C_l near the inlet and lower C_l near the outlet. Linear distribution of C_l along the axial direction of the specimen can be adopted as a simplification of this typical scenario. The distribution of $CaCO_3$ can be affected by many factors, e.g., the pH, the temperature, the additions in cementation solution, and the direction of the solution flow (Ma et al., 2022; Xiao et al., 2021b; Ma et al., 2021; Zheng et al., 2023; Cheng et al., 2019). Following the numerical biocementing scheme, specimens with different degrees of non-uniformity along the axial direction are prepared by dividing the specimen into 8 layers and inserting different numbers of cementing fines accordingly. A typical specimen with axial non-uniformity is presented in Fig. 2(a), illustrating a decreasing level of cementation from the top to the bottom of the specimen in 8 layers.

Besides the axial non-uniformity, a radial non-uniformity is expected in the immersing scheme in which the effective materials permeate into the specimen from the outer surface to the inner core, as shown in Fig. 1(b) (Li et al., 2023; Cheng et al., 2020). In contrast

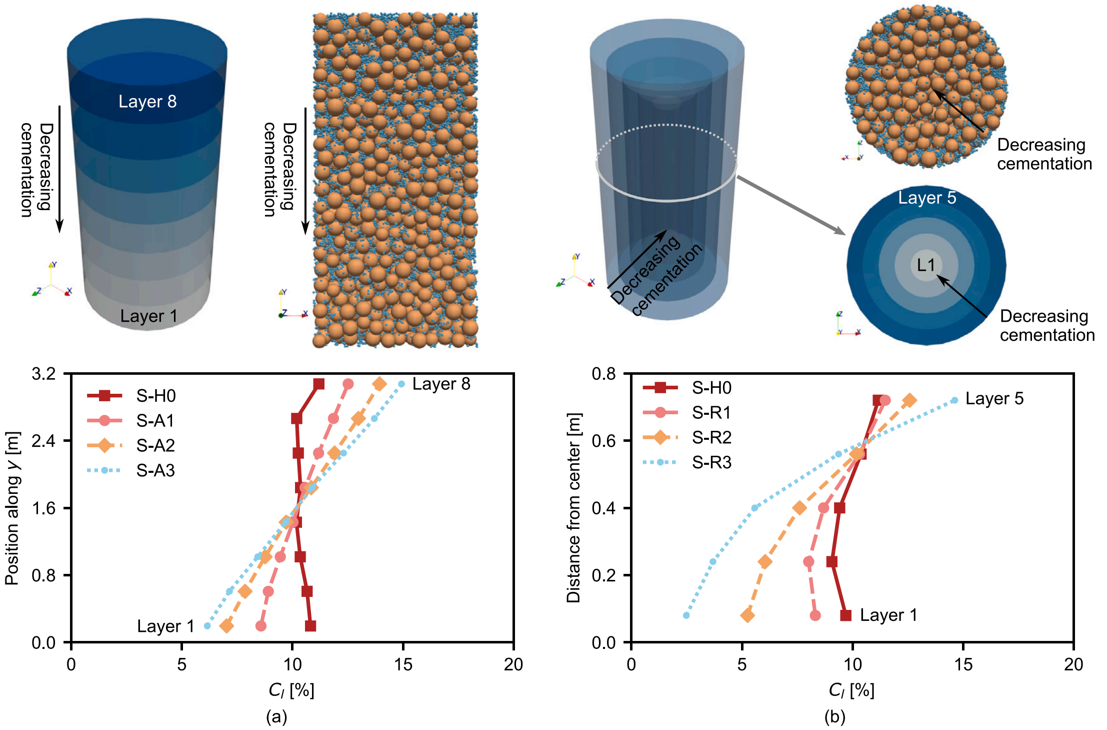

Fig. 2. Illustration of the typical specimens with non-uniform distribution of $CaCO_3$ particles and the distribution of C_l for the specimens with (a) axial non-uniformity and (b) a cemented hull.

to the well-investigated $CaCO_3$ distribution along the axial direction in the previous scenario, the $CaCO_3$ distribution along the percolation direction in this situation is not well investigated despite the report of a hard shell on the specimen surface (Li et al., 2023; Zhao et al., 2014b). From analogy to the biogrouting scheme, it is reasonable to assume a gradual reduction in C_l from the outer surface to the inner core of the specimen along the infiltration path. Specimens with different degrees of non-uniformity in this scenario are prepared by dividing the specimen into 5 layers of graded hulls whose thickness is 1/5 of the radius of the specimen and inserting different numbers of cementing fines accordingly. The distribution of $CaCO_3$ along the middle section of the specimen with graded hulls is presented in Fig. 2(b), while the sketch illustrates the decreasing cementation from the free surface to the core in 5 layers, presenting non-uniform cementation along the radial direction. These specimens are referred to as specimens with a cemented hull, in comparison with the specimens with axial non-uniformity.

It is essential to quantify the degree of non-uniformity for analyses of the effects of non-uniform biocementation. C_l for a specific region in the numerical specimen can be calculated using the mass of fines in that region and assuming a uniform pre-treatment dry density of soil particles. Then, the degree of non-uniformity can be determined as:

$$D_u = \max(C_l^i)/\min(C_l^i) \tag{8}$$

where C_l^i represents C_l for all the different layers within a specific specimen and is controlled bounded away from 0 to guarantee that the definition of D_u is physically meaningful. Notably, D_u defined here is a simple index to compare the degree of non-uniformity for layered specimens with a smooth gradient. More comprehensive descriptors under the random field model, e.g., the coefficient of variation, the characteristic length, can be further adopted to characterize the complex heterogeneity patterns in reality (Zhao et al., 2025). Three non-uniform specimens are prepared in this study for each pattern of non-uniformity. S-A1, S-A2, and S-A3 are those with axial non-uniformity with increasing D_u. The distribution of fines along the axial direction is presented in Fig. 2(a) in terms of C_l, in comparison with the uniform specimen S-H0. The 8 layers of S-H0 present largely the same C_l, while S-A3 has the highest D_u with the lowest C_l (6.6%) for the bottom layer. Meanwhile, S-R1, S-R2, and S-R3 are those with a cemented hull with increasing D_u. The distributions of fines along the radial direction are presented in Fig. 2(b) in terms of C_l, in comparison with S-H0. The uniform specimen presents largely constant C_l along the radial direction, while S-R3, with the highest D_u, has a nearly uncemented core (C_l = 2.5%).

3. Results and discussion

The mechanical responses of the specimens with the two different non-uniform patterns, i.e., those with axial non-uniformity and those with a cemented hull, are presented in this section. The roles of non-uniform biocementation on the stress–strain relation and the failure pattern in terms of particle motion are analyzed, with discussions on the global mechanical performance, the failure process, and the force chain evolution.

3.1. *Responses of specimens with axial non-uniformity*

The stress–strain relations of the three specimens with axial non-uniformity (S-A1, S-A2, and S-A3) are shown in Fig. 3(a), in comparison with S-H0. The variations of UCS and the secant modulus (E_{50}) with D_u are presented in Fig. 3(b). S-H0 has a D_u of 1.1 along the axial direction, indicating a rather uniform distribution of $CaCO_3$, and the largest D_u for the specimens with axial non-uniformity is 2.4 for S-A3. The increase in D_u leads to a quasi-linear decrease in UCS with S-H0 presenting the highest strength. As D_u increases from 1.1 for S-H0 to 2.4 for S-A3, UCS of the specimen decreases apparently from 132.1 kPa to 96.5 kPa with 27% reduction. It is interesting to note that the strength of S-A3 is apparently larger than that of the uniform specimen with the lowest C_l (6.6%), which is around 40 kPa as reported in Wu et al. (2023). Similar to strength, S-H0 presents the highest stiffness. Notably, the reduction in stiffness is not as apparent as that in strength. The smallest E_{50} is 8.35 MPa for S-A3 with the largest reduction of 9% from 9.16 MPa for S-H0.

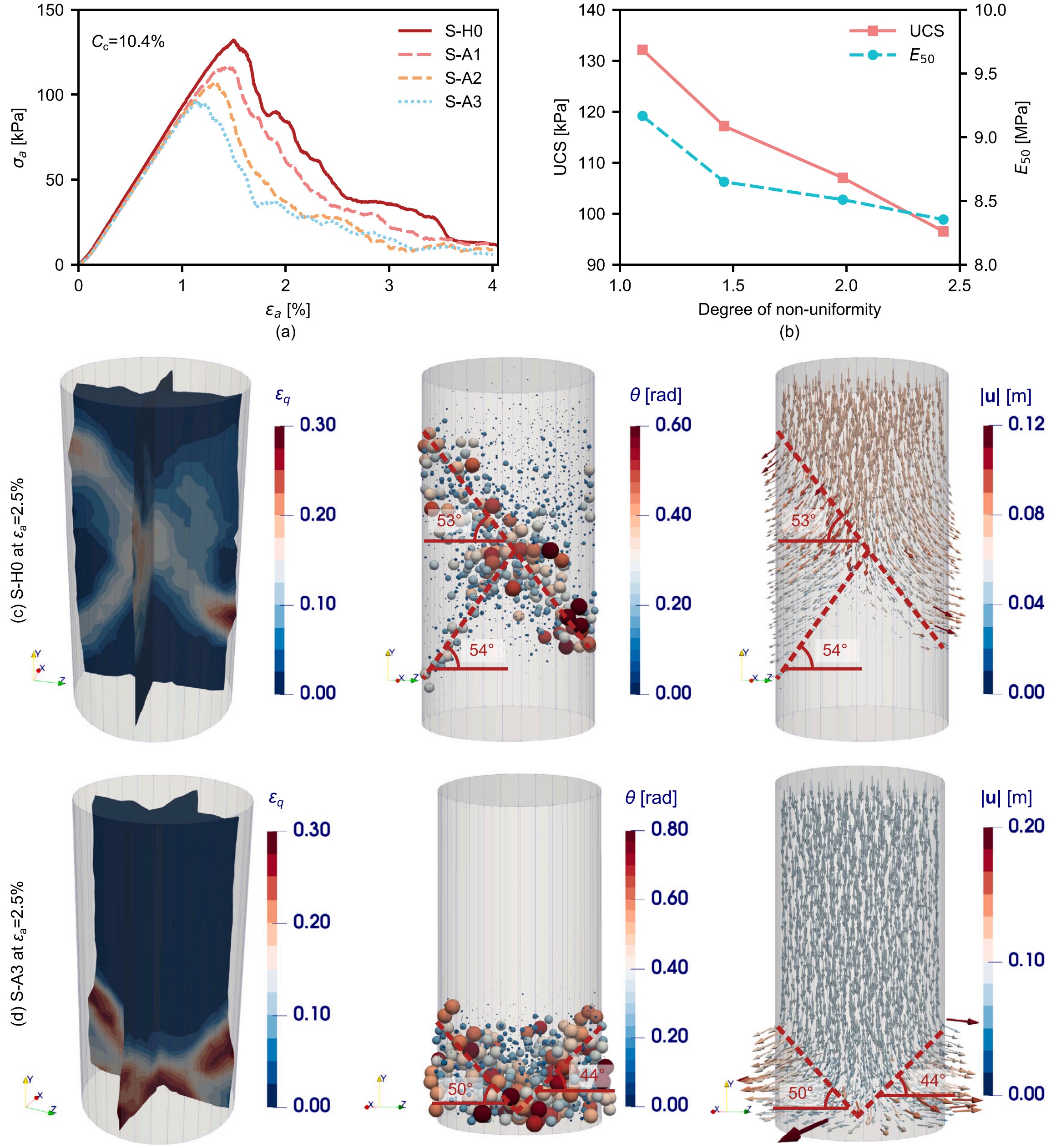

Fig. 3. Global responses of the specimens with axial non-uniformity. (a) Stress–strain relations of the specimens with various degrees of non-uniformity; (b) variations of UCS and E_{50} with D_u; failure patterns of (c) the uniform specimen S-H0 and (d) the one with high degree of non-uniformity S-A3 in terms of fields of deviatoric strain (ϵ_q), particle rotation (θ) and particle displacement (**u**).
Source: The data for S-H0 is adapted from Wu et al. (2023).

Failure mode is another significant aspect of the mechanical response and is often characterized by fields of strain and particle movement in numerical modeling. The failure patterns of the uniform specimen (S-H0) and the one with the largest D_u (S-A3) are illustrated in Fig. 3(c–d) with the fields of the deviatoric strain ϵ_q, the particle rotation θ, and the particle displacement **u**. The local strain tensor ($\boldsymbol{\epsilon}$) in DEM can be derived based on Voronoi tessellation of the sand particles in the specimen (Catalano et al., 2014). The local deviatoric strain is then derived from the microscopic strain tensor following: $\epsilon_q = \sqrt{\frac{2}{3}\mathrm{dev}\boldsymbol{\epsilon} : \mathrm{dev}\boldsymbol{\epsilon}}$, where $\mathrm{dev}\boldsymbol{\epsilon}$ is the deviatoric strain tensor and ":" represents the double contraction. The scalar field of particle rotation (θ) is illustrated with a cloud of spheres, while the radii of the spheres are scaled based on the magnitude of the particle rotation to emphasize those with large particle rotation and downplay those with small rotation. The displacement (**u**) field of the sand particles is illustrated with arrows pointing to the directions and the lengths of the arrows representing the magnitudes. Refer to Wu et al. (2023) and Catalano et al. (2014) for more detailed calculations of the relevant quantities. S-H0 presents clear T-shaped shear bands in the middle of the specimen, cutting through the specimen into several pieces, as presented in Fig. 3(c). The failure mode of S-A3 is characterized as shear bands as well. However, the failure of S-A3 is apparently localized in the lower region of the specimen, corresponding to the low-cementation layer with C_l of 6.6%. The displacement field illustrates a symmetric pattern in which the particles are squeezed out from the center of the specimen as presented in Fig. 3(d). The collaboration of the three quantities indicates that the failure of S-A3 is conical shear bands within the low-cementation region, leaving a less deformed cone in the center.

The stress–strain relations and the failure patterns presented in Fig. 3 indicate that the axial non-uniform distribution of $CaCO_3$ would affect the global mechanical responses significantly. The strength of the biocemented specimen decreases apparently with the increase in D_u. Particularly, the strength of the non-uniform specimen is smaller than the uniform specimen with the same C_c, but higher than that with the lowest C_l. The failure pattern transits from shear bands in the middle of the uniform specimen to those constrained in the low-cementation region of the non-uniform one with the increase in D_u.

3.2. Responses of specimens with a cemented hull

The stress–strain relations of the three non-uniform specimens with a cemented hull are presented in Fig. 4(a), with that of S-H0 for comparison. The variations of UCS and E_{50} with D_u are presented in Fig. 4(b). S-H0 has a D_u of 1.2 along the radial direction, suggesting a rather uniform distribution of $CaCO_3$, while the largest D_u for specimens with a cemented hull is 5.9 for S-R3. The possibility of a nearly uncemented core in the specimens with a cemented hull is the reason for the much larger D_u than those with axial non-uniformity. The strength of the uniform specimen S-H0 is still the highest. However, the decrease in strength caused by the radial non-uniformity is not as apparent as that by the axial non-uniformity. UCS decreases abruptly with the initial increase in D_u. The UCS of the specimen decreases from 132.1 kPa for S-H0 to 123.4 kPa for S-R1, presenting a 7% reduction when D_u increases from 1.2 to 1.4. However, further increase in D_u does not affect UCS apparently. As D_u increases further from 1.4 for S-R1 to 5.9 for S-R3, the UCS of the specimen decreases mildly from 123.4 kPa to 114.1 kPa. Moreover, at the same D_u, the specimen with a cemented hull presents apparently higher strength than that with axial non-uniformity. For instance, at the same D_u of 2.4, S-A3 presents a UCS of 96.5 kPa, while S-R2 presents a 24% higher UCS of 119.3 kPa. The reduction in pre-peak stiffness with D_u for the specimens with a cemented hull is modest and comparable with that for those with axial non-uniformity. S-R3 with D_u of 5.9 even presents slightly higher E_{50} than S-R2 with D_u of 2.4.

The failure patterns of the specimen with the largest D_u (S-R3) are presented in Fig. 4(c), with the fields of ϵ_q, θ, and $\mathbf{u}$. A single shear band can be identified based on the collaboration of the three quantities, cutting the specimen from the upper corner to the lower corner with a band angle of 59°. In comparison with the uniform specimen S-H0, the non-uniform specimens with a cemented hull tend to form more localized failure, with a clear shear band cutting through the specimen. Notably, a relatively diffuse failure region is observed in the center of S-R3 based on the field of particle rotation and deviatoric strain, in accordance with the low-cementation core.

Generally, the specimens with a cemented hull present better mechanical responses with apparently higher UCS and slightly higher stiffness in comparison with those with axial non-uniformity. This might be attributed to the confinement effects from the cemented hull. The initial failure of the weak core is confined by the outer strong hull and retard the global failure of the specimen. The phenomenon that the reduction in strength does not vary significantly with the increase in D_u is possibly caused by the competition between the increase in the confinement from the cemented hull and the reduction in strength of the low-cementation core. In contrast, the local failure of the weak layer dominates the global failure of the specimens with axial non-uniformity. The detailed failure process and mechanism of the specimens with the two patterns of non-uniformity will be discussed in the following sections.

3.3. Temporal and spatial evolution of debonding events

The debonding responses are the key factors to characterize the failure mechanism of cohesive granular materials. The normalized debonding number of different regions can be determined as: $\hat{N} = N/N_b$, where N is the number of broken bonds and N_b is the total number of bonds in that region. The evolution of $\hat{N}$ with ϵ_a for the typical specimens is presented in Fig. 5. The evolution for S-H0 is presented for reference with layers partitioned along the axial direction in Fig. 5(a) and along the radial direction in Fig. 5(c). The vertical dashed lines indicate the ϵ_a of the peak stress. The total debonding number decreases apparently for the specimens with high degree of non-uniformity, in line with the apparent reduction in UCS.

In terms of the role of axial non-uniformity, the distribution of debonding events for S-H0 is largely symmetric as presented in Fig. 5(a). Layers 4 and 5 present the most debonding events, followed by Layers 3 and 6. Specifically, the layers close to the loading plates present marginal debonding events. In terms of the role of radial non-uniformity, the distribution of debonding events for all 5 layers along the radial direction presents similar pre-peak responses in terms of $\hat{N}$ with marginal debonding events, distributed evenly among the specimen, as presented in Fig. 5(c). The inner core (Layers 1, 2, and 3) presents higher $\hat{N}$ at the post-peak stage due to the intersection of the conjugated shear bands. The locations of the debonding events are presented in Fig. 6(a) with the color of the dots indicating the ϵ_a at which the debonding events occur. Specifically, the middle inset displays the debonding events immediately after the stress peak. The pre-peak debonding events, as presented in the left inset, distribute evenly among the whole specimen as the precursor of the following shear bands, while marginally near the upper and lower loading plates, in line with the evolution of $\hat{N}$ in Fig. 5(a). Immediately after the stress peak, a large number of debonding events occur in the middle of the specimen, as presented in the middle inset. The large number of debonding events in light green agrees with the dominance of the shear band with a band angle of 53°. While the debonding events in dark blue in the upper region of the specimen suggest the precursor of a new shear band. The debonding events at $\epsilon_a = 2.1$–2.5%, as presented in the right inset, present the concurrent development of the major branch with a band angle of 53° and the minor branch with a band angle of 54°. The diffusive distribution of debonding events at the upper right corner suggests a rather complex failure in that region without a mature shear band.

For S-A3 with a high degree of axial non-uniformity, the distribution of the debonding events is rather asymmetrical, with dominance of debonding in the lower region with less cementation, as presented in Fig. 5(b). The failure of S-A3 is dominated by the debonding events at the bottom two layers (Layers 1 and 2) with moderate debonding events at Layer 3. Specifically, Layers 1 and 2 present a linear increase in $\hat{N}$ to 0.2 immediately after the stress peak and then increase gradually to constant values around 0.26. The evolution of $\hat{N}$ suggests that more than a quarter of the bonds are broken in the two weak layers. The spatial evolution of the debonding events within S-A3 is presented in Fig. 6(b). Despite the illustration of the shear bands identified from the fields of ϵ_q, θ, and $\mathbf{u}$, the locations of the debonding events themselves cannot illustrate the shear bands clearly. All the pre-peak debonding events are located in the lower half of the specimen, and those in the upper half are rare exceptions. Despite the conical shear bands, the debonding events distribute evenly along the radial direction without clear identification of an intact cone-shaped region. It suggests that the bottom layers of the specimen are damaged under axial loading due to the relatively weak cementation, and the cone-shaped region with small strain is attributed to the constraint from the intact upper layers and the bottom plate.

For S-R3 with a high degree of radial non-uniformity, Layers 1, 2, and 3 lead the failure process due to the weakly-cemented core. The increases in $\hat{N}$ for Layers 4 and 5 are delayed due to the higher cementation in the hull. It is the failure in Layers 4 and 5 that determines the global failure of this non-uniform specimen. Recall that $\hat{N}$ is a normalized value by dividing the debonding number by the total bond number in the corresponding region, the debonding events in the outer Layers 4 and 5 are actually much more than those in the inner core.

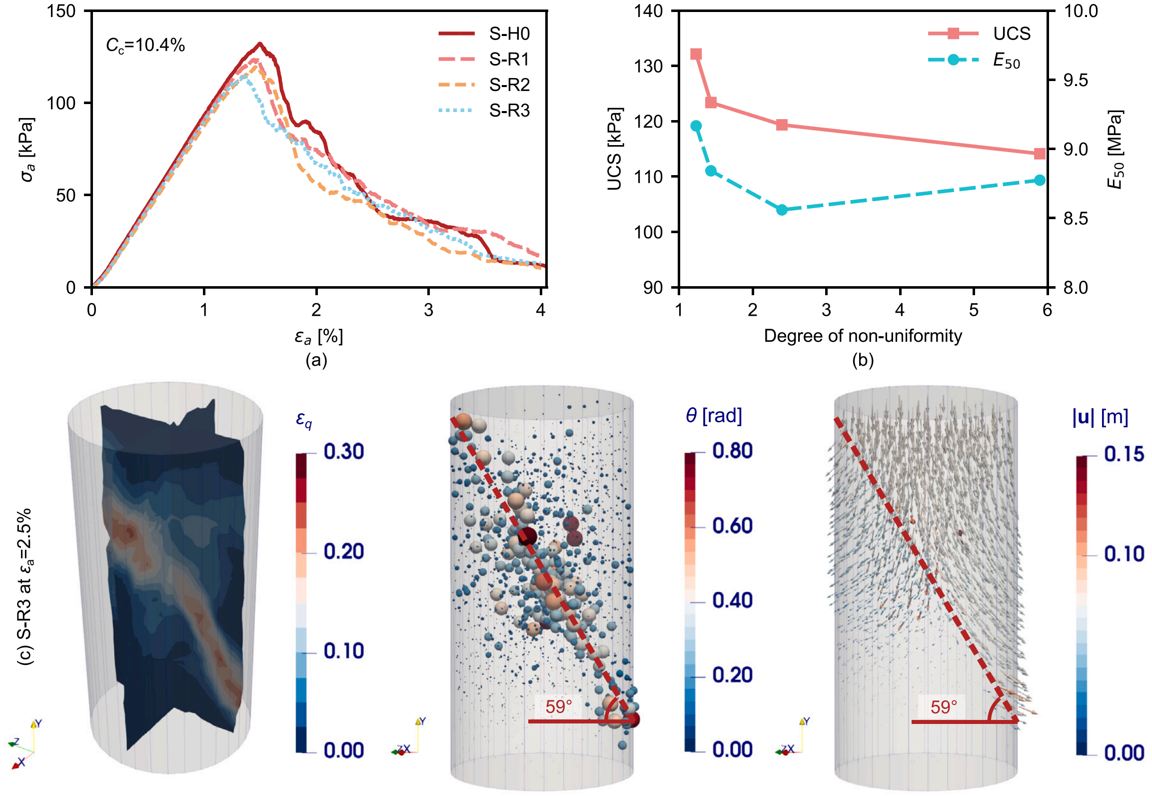

Fig. 4. Global responses of the specimens with a cemented hull. (a) Stress–strain relations of the specimens with various degrees of non-uniformity; (b) variations of UCS and E_{50} with D_u; (c) failure patterns of the one with high degree of non-uniformity S-R3 in terms of fields of deviatoric strain (ϵ_q), particle rotation (θ) and particle displacement (**u**).
Source: The data for S-H0 is adapted from Wu et al. (2023).

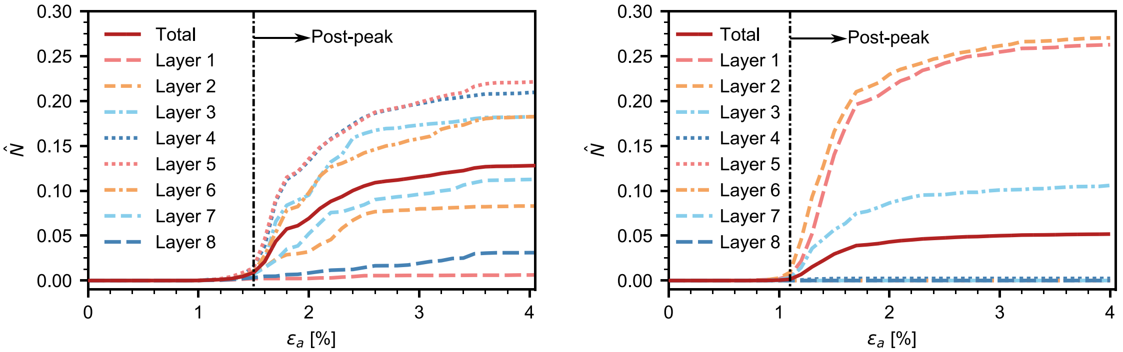

(a) S-H0 partitioned axially (b) S-A3

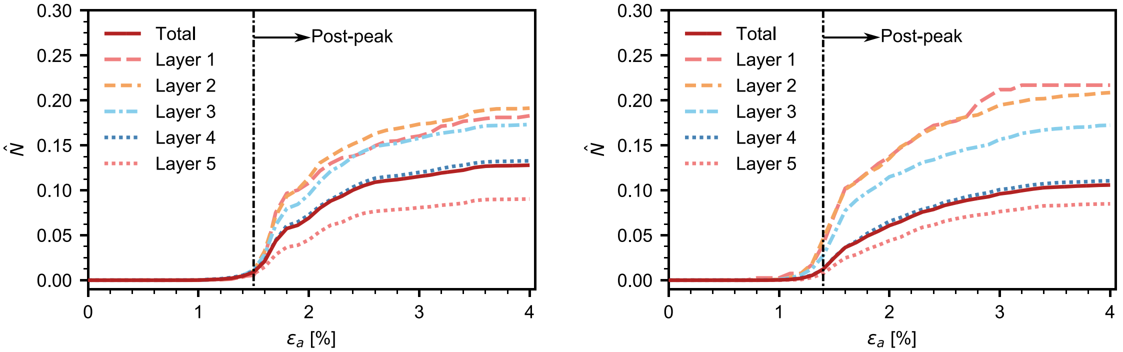

(c) S-H0 partitioned radially (d) S-R3

Fig. 5. The temporal evolution of normalized debonding number ($\hat{N}$) with increasing ϵ_a for the typical specimens.

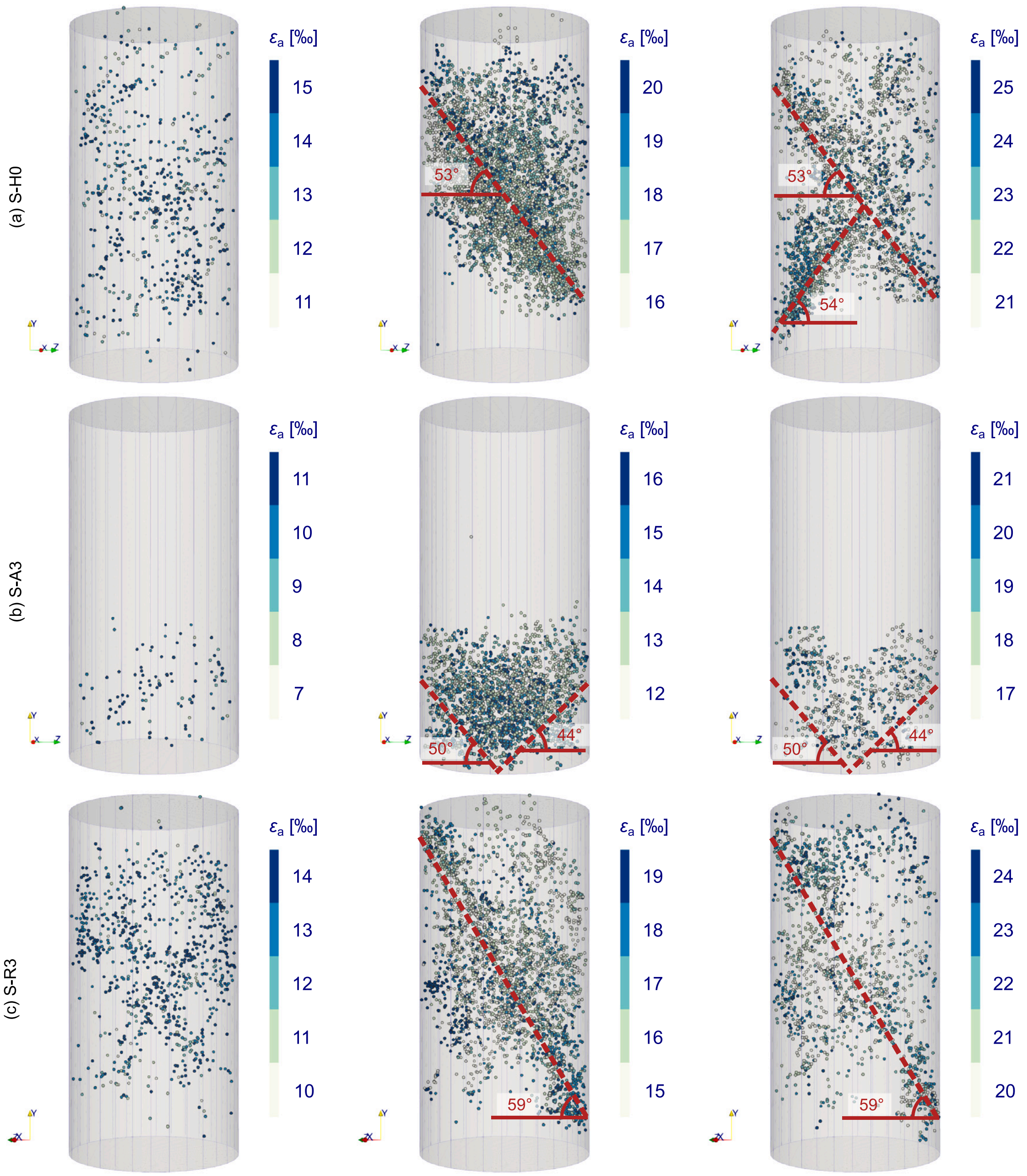

Fig. 6. The spatial evolution of debonding events for the typical specimens. Each subfigure presents the locations of debonding events within an axial strain increment of 5‰ and the color of the dots indicates the axial strain level at which the debonding events occur.

The spatial evolution of the debonding events in S-R3 is presented in Fig. 6(c). The debonding events in light green in the upper right corner in the middle inset indicate a premature shear band, besides the shear band with a band angle of 59°. But the lack of debonding events in dark blue there and the deformation patterns in Fig. 4 suggest that the development of this branch of shear band is inhibited while the branch along the observing direction dominates the failure process. Notably, the shear bands are relatively thin in comparison with S-H0, suggesting a more brittle failure pattern.

3.4. Evolution of contact-based anisotropy

The interparticle contact system and its anisotropy is useful for analyzing and understanding the deformation mechanism of granular materials. Considering the large number of fines and their roles to provide cohesion for the structure, the focus is put on the interparticle contacts between sand particles herein. The contact-based fabric is a convenient way to characterize the microscopic evolution of the interparticle contact system. The contact-normal-based fabric tensor can be defined following Guo and Zhao (2014) and Oda (1982): $\boldsymbol{\psi} = \frac{1}{N_c}\sum \mathbf{n}^c \otimes \mathbf{n}^c$, where N_c is the number of sand-sand contacts in the region of interest, $\mathbf{n}^c$ is the contact normal vector for a sand-sand contact, and '$\otimes$' is the dyadic operator. Furthermore, the anisotropic intensity of the interparticle contact system in 3D can be quantified with a scalar: $F_a = \sqrt{3/2\mathbf{F}_a : \mathbf{F}_a}$, where $\mathbf{F}_a = 15/2\mathrm{dev}\boldsymbol{\psi}$ is the deviatoric fabric tensor, and ':' denotes the double contraction operator (Guo and Zhao, 2016).

The evolution of the anisotropic intensity for the typical specimens is presented in Fig. 7. Unlike the good correlation between anisotropic intensity and deviatoric stress for noncohesive granular material under

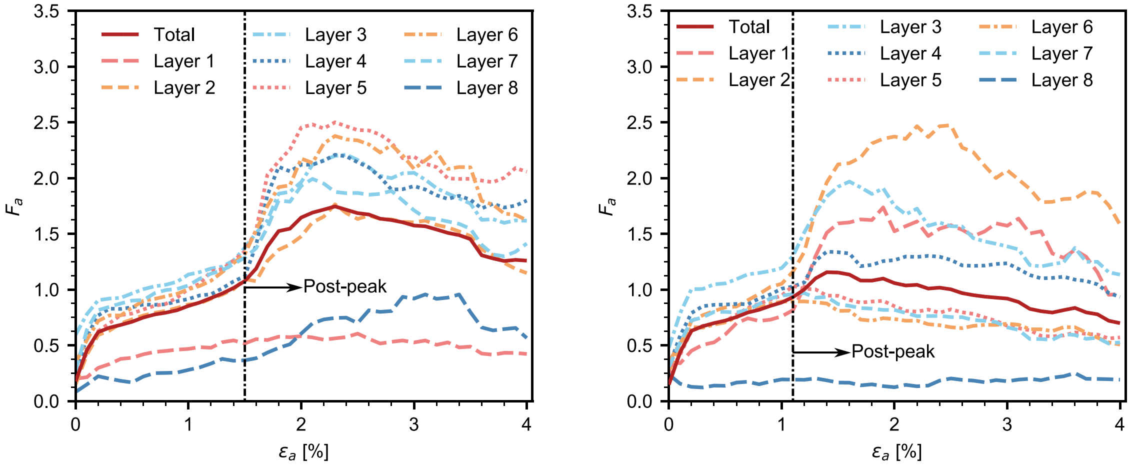

(a) S-H0 partitioned axially (b) S-A3

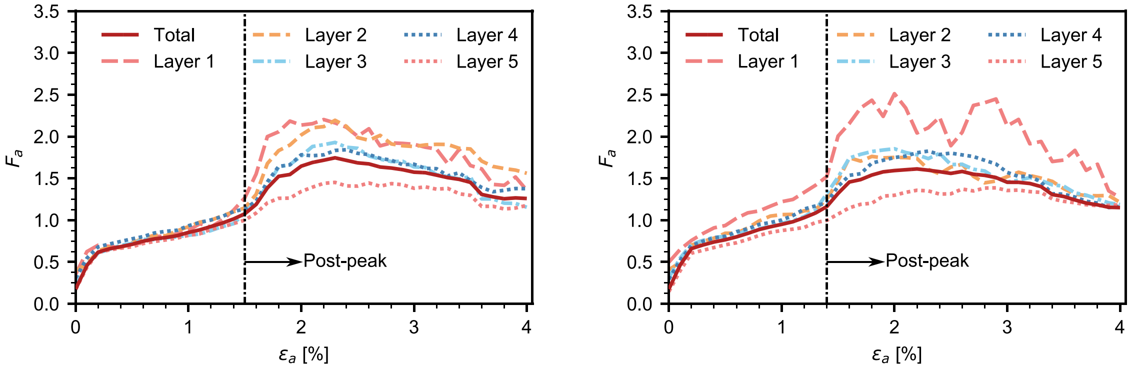

(c) S-H0 partitioned radially (d) S-R3

Fig. 7. The evolution of anisotropic intensity with axial strain for the typical specimens.

confinement (Guo and Zhao, 2013), the evolution of F_a herein presents distinct features from the stress–strain relations. In terms of the role of axial non-uniformity, F_a of most layers in S-H0 present trends similar to the total F_a, where F_a increases rapidly at the initial stage and then increases mildly to the peak-stress state. A second surge in F_a is noted after the peak stress, which is related to the burst in debonding events and the corresponding redistribution of the contact force from the initial cohesion-dominated framework to the post-failure friction-dominated structure. F_a increases rapidly to a peak and then decreases gradually due to the intense reduction in stress at the post-peak stage. Notably, the two layers close to the loading plates (Layers 1 and 8) presented a marginal increase in F_a due to the marginal debonding events and the lateral constraints from the loading plates. For S-A3 with a high degree of axial non-uniformity, F_a for the lower half of the specimen presents trends similar to S-H0, with a second increase after the stress peak due to the debonding process. In contrast, F_a for the upper half of the specimen decreases directly after the stress peak due to the local unloading process and the few debonding events.

The evolution of the anisotropic intensity in terms of the role of radial non-uniformity is presented in Fig. 7(c–d). Generally, the trends of F_a for the two specimens are similar, with an initial rapid increase followed by a gradual growth at the pre-peak stage and a second increase with a gradual decrease at the post-peak stage. The different layers of S-H0 present similar pre-peak responses, while the inner core displays slightly higher F_a at the post-peak stage. For S-R3, the innermost layer (Layer 1) presents the highest F_a from the initial state, due to the initial insufficient cementation, while the outer hull (Layer 5) presents the lowest F_a. Moreover, the fluctuations for Layer 1 at the post-peak stage are a distinct feature from other layers, possibly due to insufficient cementation and the consequent unstable evolution of the force chain network.

3.5. Force chain network

While the evolution of F_a depicts a global picture, it is more intuitive to observe the force chain network at key stages directly. The evolution of the force chain network for the typical specimens is illustrated through snapshots at the peak-stress state, the peak-anisotropy state, and the final state in Fig. 8. The contact forces between coarse particles are presented with cylinders, and the color of the cylinder represents the magnitude of the force. Note that the diameter of the cylinder is adjusted for a better presentation of the individual insets and is not strictly proportional to the magnitude among different snapshots. For the uniform specimen S-H0, the force chain network at the peak-stress state presents strong force chains with dark color distributed uniformly among the specimen without apparent localization. Moreover, the strong force chains present clear dominance along the vertical direction, while the weak ones present various directions. At the peak-anisotropy state, the magnitude of the contact forces reduces and the number of strong forces decreases apparently with apparent localization in the shear bands. At the final state, the magnitude of the contact forces and the number of strong forces decrease further due to the coupling effects of the post-peak reduction in axial stress and the degradation of the microstructure. The development of the shear band leads to the formation of the upper and the lower pyramids contacting in the middle of the specimen. A clear force chain can be noted from the top plate to the bottom plate through the center of the specimen.

The force chain networks for S-A3 with a high degree of axial non-uniformity are presented in Fig. 8(b). The force chain network at the peak stress state is similar to that of S-H0, while the concentration of strong forces in the weak layers near the bottom plate is noted. The force chain network at the peak-anisotropy state is distinct from that of S-H0, with apparent strong forces in the lower part of the specimen.

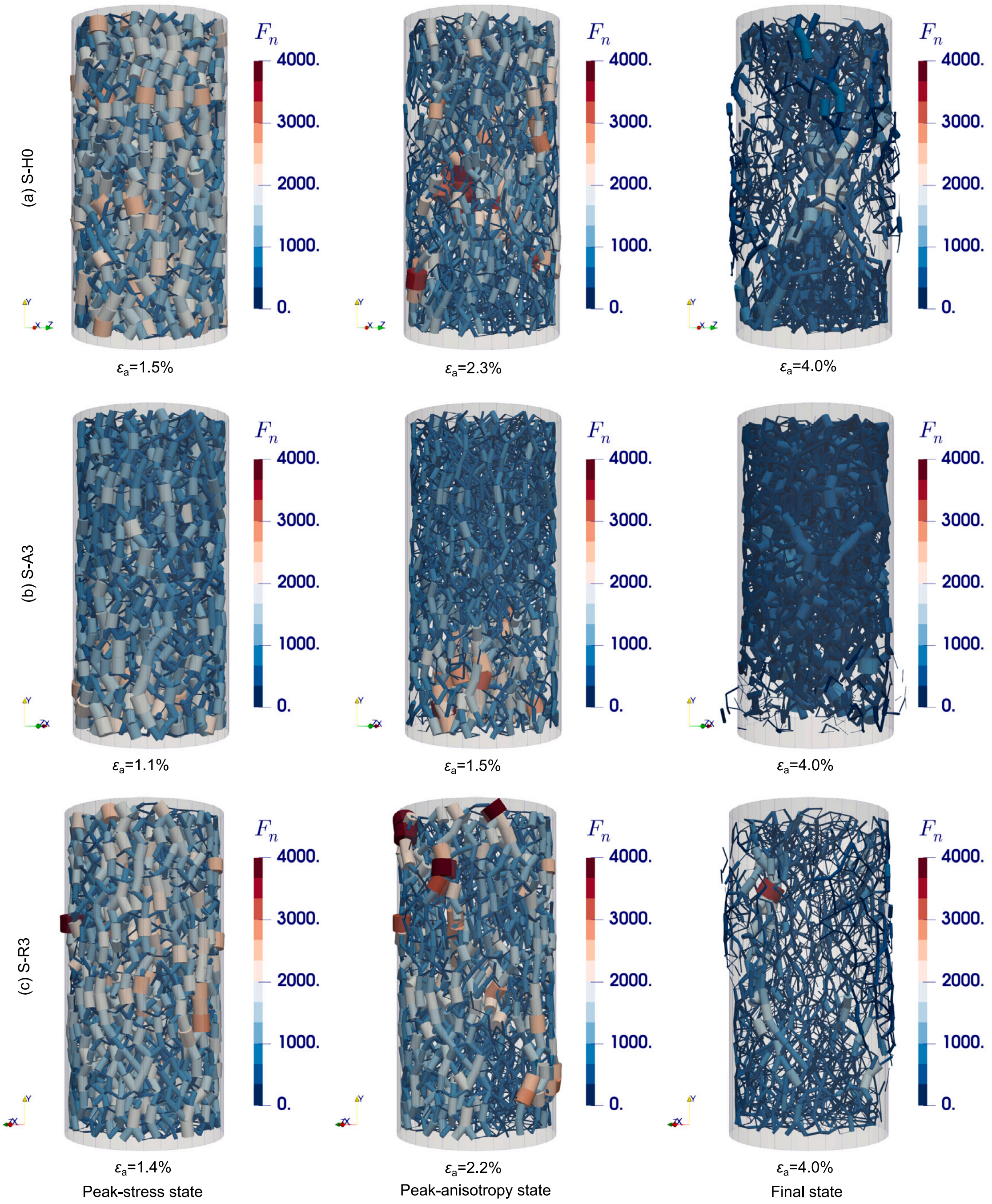

Fig. 8. The force chain network of the typical specimens at key stages.

At the final state, a relatively sparse force chain network is noted in the weak layer, mainly due to the microstructural degradation of the weakly-cemented zone. The force chain networks for S-R3 with a high degree of radial non-uniformity are presented in Fig. 8(c). The force chain networks at different states are largely the same as those of S-H0. At the peak-anisotropy state, clear alignment of the vertical strong forces in the shear band is observed. This phenomenon can be explained by the intense in-band debonding events and the corresponding post-failure contacts between the coarse particles (Wu et al., 2020b). The force chain network at the final state presents a chain of strong forces from the top to the bottom, penetrating the specimen along the axial direction, with local intensity crossing the shear band region.

3.6. *Practical implications*

The 3D DEM modeling indicates that the uniform specimen has the highest strength and stiffness among all the investigated cases, which suggests that it is beneficial to explore advanced biocementation techniques to improve the uniformity of $CaCO_3$ precipitation in order to improve the mechanical performance. Notably, Eq. (8) can be readily generalized for the quantitative assessment of the degree of non-uniformity in practical applications with local $CaCO_3$ content (C_l) by sampling from different regions. Considering the practical applicability, the biogrouting scheme has better potential for field implementation. As reviewed by Zheng et al. (2023), various attempts have been made to mitigate the non-uniform distribution of $CaCO_3$ precipitation, and these attempts can be assorted into the methods to assist bacterial adsorption in the two-phase techniques, and the methods to delay the formation of $CaCO_3$ in the one-phase techniques. Although element-scale experiments are widely adopted to compare the mechanical performance among different techniques, the degree of non-uniformity might be underestimated given the much larger scale for the field applications. From a practical point of view, it is of special interest to measure the distribution of C_l along the grouting direction at the larger scale (Yang et al., 2023), and evaluate D_u based on the distribution of C_l. The good correlation between D_u and the mechanical performance in this study provides a basis to estimate the larger-scale mechanical responses. Besides, another valuable insight from the numerical modeling would be the reasonable range for estimating the strength of the biocemented specimen. The UCS of the non-uniform specimen with axial non-uniformity would be lower than that of the uniform specimen with the global $CaCO_3$ content (C_c), and higher than that of the uniform one with the minimum local $CaCO_3$ content ($\min(C_l)$).

For the specimen with axial non-uniformity, an increase in D_u significantly reduces its mechanical performance. In contrast, an increase in D_u does not affect the mechanical responses significantly for the specimens with a cemented hull. Based on the same C_c, the specimens with a cemented hull generally have higher strength and stiffness than those with axial non-uniformity. This implies that the techniques tending to form specimens with a cemented hull, e.g., the soaking or immersing methods, have a higher efficiency in comparison with those tending to form axial non-uniformity, e.g., the biogrouting methods. Hence, the soaking or immersing methods might be more appropriate for bio-construction with MICP (Liu et al., 2023). It is beneficial to form bricks and other construction members in the factory through the premixing and immersing methods (Liu et al., 2021). The cemented hulls can protect the construction members effectively and provide enhanced mechanical performance. Moreover, it is reasonable to conduct a quick judgment of the uniformity for element-scale experiments, by observing the failure pattern of the specimen (Mori and Uday, 2022). Those presenting global failure with shear bands are likely to possess a relatively uniform distribution of $CaCO_3$, while those presenting local failure may have defects and increase the dispersion of the experimental results.

4. Conclusions

This study presents a 3D DEM modeling of the non-uniform biocementation with cementing fines representing the $CaCO_3$ crystals. The focus has been put on a widespread phenomenon in biocemented sand, i.e., the non-uniform distribution of the $CaCO_3$ precipitation. Two typical distribution patterns frequently observed in element-scale specimens are reproduced: one exhibiting axial non-uniformity and the other featuring a cemented hull. The global mechanical responses and the failure mechanisms of the specimens with various degrees of non-uniformity are investigated in an a priori manner, and the major findings are summarized below.

(a) The uniform specimen has the best global mechanical response, with the largest strength and stiffness. The mechanical performance of specimens with axial non-uniformity is more sensitive to the degree of non-uniformity than that of those with a cemented hull. The specimens with a cemented hull generally present much better global mechanical responses than those with axial non-uniformity.

(b) The debonding events of the specimens with axial non-uniformity tend to localize in the weakly-cemented layers. In contrast, the debonding events in the specimens with a cemented hull start from the weakly-cemented core, followed by those in the cemented hull. The confinement effects from the cemented hull upon the initial damage in the weakly-cemented core are attributed to the better global mechanical performance of the specimens with a cemented hull.

(c) The specimens with a cemented hull present clear shear bands cutting through the specimens, which is similar to the uniform one. The larger band angle and the thinner band width suggest a more brittle behavior. In contrast, the specimens with axial non-uniformity present localized failure in the weakly-cemented layers. The one with a high degree of axial non-uniformity even forms conical shear bands and a cone-shaped region with small strain in the highly-damaged weakly cemented layers, under the constraint of the intact upper layer and the bottom loading plate.

(d) The overall evolution of the contact-based anisotropy presents a rapid increase at the initial stage and a mild increase thereafter to the peak-stress state, followed by a second surge to the peak-anisotropy state and a mild decrease thereafter. The different regions of the uniform specimen present similar trends, except for the layers close to the loading plate. The weakly-cemented layers dominate the high-anisotropy regions for the specimens with axial non-uniformity, with highly concentrated strong contact forces. The specimens with a cemented hull are similar to the uniform one in this aspect, with fluctuations of the anisotropic intensity in the weakly cemented core suggesting a less stable force chain network.

The influence of non-uniform biocementation on the mechanical responses of biocemented soils is investigated through 3D DEM modeling in this study by modeling the two typical ideal distribution patterns of $CaCO_3$ crystals in element-scale specimens with cementing fines. The actual distribution of $CaCO_3$ crystals might be more complex, which can be identified through advanced examination techniques like CT scanning (Dadda et al., 2019). Moreover, this study focuses on the non-uniform distribution of $CaCO_3$ at the element scale. The non-uniformity in the field applications might be more severe and affect the performance of the MICP techniques. This scenario can be further investigated through multiscale modeling methods, e.g., FEM×DEM (Wu et al., 2018a) or MPM×DEM modeling (Liang et al., 2023).

CRediT authorship contribution statement

Huanran Wu: Writing – original draft, Methodology, Conceptualization. **Yang Xiao:** Writing – review & editing, Validation, Investigation. **Weijian Liang:** Writing – review & editing, Validation, Investigation. **Jidong Zhao:** Writing – review & editing, Validation, Investigation. **T. Matthew Evans:** Writing – review & editing, Validation, Investigation.

Declaration of competing interest

The authors declare that they have no known competing financial interests or personal relationships that could have appeared to influence the work reported in this paper.

Acknowledgments

The author would like to acknowledge the financial support from the National Natural Science Foundation of China (Grant No. 42377155, and 52425806) and the Fundamental Research Funds for the Central Universities, China (Grant No. 2024IAIS-ZX004).

Data availability

Data will be made available on request.

References

Ahenkorah, I., Rahman, M.M., Karim, M.R., Beecham, S., 2024. Characteristics of MICP- and EICP-treated sands in simple shear conditions: A benchmarking with the critical state of untreated sand. Géotechnique 74, 1649–1663. http://dx.doi.org/10.1680/jgeot.22.00329.

Catalano, E., Chareyre, B., Barthélémy, E., 2014. Pore-scale modeling of fluid-particles interaction and emerging poromechanical effects. Int. J. Numer. Anal. Methods Geomech. 38, 51–71. http://dx.doi.org/10.1002/nag.2198.

Cheng, L., Kobayashi, T., Shahin, M.A., 2020. Microbially induced calcite precipitation for production of "bio-bricks" treated at partial saturation condition. Constr. Build. Mater. 231, 117095. http://dx.doi.org/10.1016/j.conbuildmat.2019.117095.

Cheng, L., Shahin, M.A., Chu, J., 2019. Soil bio-cementation using a new one-phase low-pH injection method. Acta Geotech. 14, 615–626. http://dx.doi.org/10.1007/s11440-018-0738-2.

Choi, S.G., Chang, I., Lee, M., Lee, J.H., Han, J.T., Kwon, T.H., 2020. Review on geotechnical engineering properties of sands treated by microbially induced calcium carbonate precipitation (MICP) and biopolymers. Constr. Build. Mater. 246, 118415. http://dx.doi.org/10.1016/j.conbuildmat.2020.118415.

Cui, M.J., Lai, H.J., Hoang, T., Chu, J., 2021. One-phase-low-pH enzyme induced carbonate precipitation (EICP) method for soil improvement. Acta Geotech. 16, 481–489. http://dx.doi.org/10.1007/s11440-020-01043-2.

Cui, M.J., Lai, H.J., Wu, S.F., Chu, J., 2024. Comparison of soil improvement methods using crude soybean enzyme, bacterial enzyme or bacteria-induced carbonate precipitation. Géotechnique 74, 18–26. http://dx.doi.org/10.1680/jgeot.21.00131.

Dadda, A., Geindreau, C., Emeriault, F., Rolland du Roscoat, S., Esnault Filet, A., Garandet, A., 2019. Characterization of contact properties in biocemented sand using 3D X-ray micro-tomography. Acta Geotech. 14, 597–613. http://dx.doi.org/10.1007/s11440-018-0744-4.

DeJong, J.T., Mortensen, B.M., Martinez, B.C., Nelson, D.C., 2010. Bio-mediated soil improvement. Ecol. Eng. 36, 197–210. http://dx.doi.org/10.1016/j.ecoleng.2008.12.029.

Dejong, J., Soga, K., Kavazanjian, E., Burns, S., Van Paassen, L., Al Qabany, A., Aydilek, A., Bang, S., Burbank, M., Caslake, L., Chen, C., Cheng, X., Chu, J., Ciurli, S., Esnault-Filet, A., Fauriel, S., Hamdan, N., Hata, T., Inagaki, Y., Jefferis, S., Kuo, M., Laloui, L., Larrahondo, J., Manning, D., Martinez, B., Montoya, B., Nelson, D., Palomino, A., Renforth, P., Santamarina, J., Seagren, E., Tanyu, B., Tsesarsky, M., Weaver, T., 2013. Biogeochemical processes and geotechnical applications: Progress, opportunities and challenges. Géotechnique 63, 287–301. http://dx.doi.org/10.1680/geot.SIP13.P.017.

Evans, T.M., Khoubani, A., Montoya, B.M., 2015. Simulating mechanical response in bio-cemented sands. In: Computer Methods and Recent Advances in Geomechanics: Proceedings of the 14th International Conference of International Association for Computer Methods and Recent Advances in Geomechanics, 2014 (IACMAG 2014). Taylor & Francis Books Ltd, pp. 1569–1574.

Feng, K., 2015. Constitutive Response of Microbial Induced Calcite Precipitation Cemented Sands (Doctor of Philosophy). North Carolina State University, Raleigh.

Feng, K., Montoya, B.M., 2016. Influence of confinement and cementation level on the behavior of microbial-induced calcite precipitated sands under monotonic drained loading. J. Geotech. Geoenvironmental Eng. 142, 04015057. http://dx.doi.org/10.1061/(ASCE)GT.1943-5606.0001379.

Feng, K., Montoya, B.M., Evans, T.M., 2017. Discrete element method simulations of bio-cemented sands. Comput. Geotech. 85, 139–150. http://dx.doi.org/10.1016/j.compgeo.2016.12.028.

Fu, T., Haigh, S.K., 2024. Biocementation of a well-graded gravelly soil and macromechanical characterization. J. Geotech. Geoenvironmental Eng. 150, 04024061. http://dx.doi.org/10.1061/JGGEFK.GTENG-12091.

Gao, K., Lin, H., Suleiman, M.T., Bick, P., Babuska, T., Li, X., Helm, J., Brown, D.G., Zouari, N., 2023. Shear and tensile strength measurements of CaCO3 cemented bonds between glass beads treated by microbially induced carbonate precipitation. J. Geotech. Geoenvironmental Eng. 149, 04022117. http://dx.doi.org/10.1061/(ASCE)GT.1943-5606.0002927.

Ghasemi, P., Montoya, B.M., 2022. Field implementation of microbially induced calcium carbonate precipitation for surface erosion reduction of a coastal plain sandy slope. J. Geotech. Geoenvironmental Eng. 148, 04022071. http://dx.doi.org/10.1061/(ASCE)GT.1943-5606.0002836.

Gong, L., Liu, L., Xu, Y., Zhu, S., Hao, T., 2023. A discrete element simulation considering calcite crystal shape to investigate the mechanical behaviors of bio-cemented sands. Constr. Build. Mater. 368, 130398. http://dx.doi.org/10.1016/j.conbuildmat.2023.130398.

Guo, N., Zhao, J., 2013. The signature of shear-induced anisotropy in granular media. Comput. Geotech. 47, 1–15. http://dx.doi.org/10.1016/j.compgeo.2012.07.002.

Guo, N., Zhao, J., 2014. A coupled FEM/DEM approach for hierarchical multiscale modelling of granular media. Internat. J. Numer. Methods Engrg. 99, 789–818. http://dx.doi.org/10.1002/nme.4702.

Guo, N., Zhao, J., 2016. 3D multiscale modeling of strain localization in granular media. Comput. Geotech. 80, 360–372. http://dx.doi.org/10.1016/j.compgeo.2016.01.020.

Ham, S.M., Martinez, A., Han, G., Kwon, T.H., 2022. Grain-scale tensile and shear strengths of glass beads cemented by MICP. J. Geotech. Geoenvironmental Eng. 148, 04022068. http://dx.doi.org/10.1061/(ASCE)GT.1943-5606.0002863.

Ivanov, V., Chu, J., 2008. Applications of microorganisms to geotechnical engineering for bioclogging and biocementation of soil in situ. Rev. Environ. Sci. Bio/Technol. 7, 139–153. http://dx.doi.org/10.1007/s11157-007-9126-3.

Konstantinou, C., Wang, Y., Biscontin, G., 2023. A systematic study on the influence of grain characteristics on hydraulic and mechanical performance of MICP-treated porous media. Transp. Porous Media 147, 305–330. http://dx.doi.org/10.1007/s11242-023-01909-5.

Lai, H.J., Cui, M.J., Chu, J., 2023. Effect of pH on soil improvement using one-phase-low-pH MICP or EICP biocementation method. Acta Geotech. 18, 3259–3272. http://dx.doi.org/10.1007/s11440-022-01759-3.

Li, Y., Li, Y., Guo, Z., Xu, Q., 2023. Durability of MICP-reinforced calcareous sand in marine environments: Laboratory and field experimental study. Biogeotechnics 1, 100018. http://dx.doi.org/10.1016/j.bgtech.2023.100018.

Liang, W., Zhao, J., Wu, H., Soga, K., 2023. Multiscale, multiphysics modeling of saturated granular materials in large deformation. Comput. Methods Appl. Mech. Engrg. 405, 115871. http://dx.doi.org/10.1016/j.cma.2022.115871.

Liu, H., Chu, J., Kavazanjian, E., 2023. Biogeotechnics: A new frontier in geotechnical engineering for sustainability. Biogeotechnics 1, 100001. http://dx.doi.org/10.1016/j.bgtech.2023.100001.

Liu, S., Du, K., Huang, W., Wen, K., Amini, F., Li, L., 2021. Improvement of erosion-resistance of bio-bricks through fiber and multiple MICP treatments. Constr. Build. Mater. 271, 121573. http://dx.doi.org/10.1016/j.conbuildmat.2020.121573.

Liu, Q., Ghasemi, P., Montoya, B.M., Lajoie, C.A., Kelly, C.J., Evans, T.M., 2025. Upscaling bacterial inoculation for field-scale applications of microbially induced carbonate precipitation. J. Mater. Civ. Eng. 37, 06024008. http://dx.doi.org/10.1061/JMCEE7.MTENG-18400.

Liufu, Z., Yuan, J., Shan, Y., Cui, J., Tong, H., Zhao, J., 2023. Effect of particle size and gradation on compressive strength of MICP-treated calcareous sand. Appl. Ocean Res. 140, 103723. http://dx.doi.org/10.1016/j.apor.2023.103723.

Ma, G., He, X., Jiang, X., Liu, H., Chu, J., Xiao, Y., 2021. Strength and permeability of bentonite-assisted biocemented coarse sand. Can. Geotech. J. 58, 969–981. http://dx.doi.org/10.1139/cgj-2020-0045.

Ma, G., Xiao, Y., He, X., Li, J., Chu, J., Liu, H., 2022. Kaolin-nucleation-based biotreated calcareous sand through unsaturated percolation method. Acta Geotech. 17, 3181–3193. http://dx.doi.org/10.1007/s11440-022-01459-y.

Mitchell, J.K., Santamarina, J.C., 2005. Biological considerations in geotechnical engineering. J. Geotech. Geoenvironmental Eng. 131, 1222–1233. http://dx.doi.org/10.1061/(ASCE)1090-0241(2005)131:10(1222).

Montoya, B.M., DeJong, J.T., 2015. Stress-strain behavior of sands cemented by microbially induced calcite precipitation. J. Geotech. Geoenvironmental Eng. 141, 04015019. http://dx.doi.org/10.1061/(ASCE)GT.1943-5606.0001302.

Montoya, B., Dejong, J., Boulanger, R., 2013. Dynamic response of liquefiable sand improved by microbial-induced calcite precipitation. Géotechnique 63, 302–312. http://dx.doi.org/10.1680/geot.SIP13.P.019.

Mori, D., Uday, K.V., 2022. Enhancing soil strength at targeted calcite content via optimizing chemical application parameters using Taguchi Method for biocementation. J. Geotech. Geoenvironmental Eng. 148, 04022031. http://dx.doi.org/10.1061/(ASCE)GT.1943-5606.0002805.

Nafisi, A., Montoya, B.M., Evans, T.M., 2020. Shear strength envelopes of biocemented sands with varying particle size and cementation level. J. Geotech. Geoenvironmental Eng. 146, 04020002. http://dx.doi.org/10.1061/(ASCE)GT.1943-5606.0002201.

Oda, M., 1982. Fabric tensor for discontinuous geological materials. Soils Found. 22, 96–108. http://dx.doi.org/10.3208/sandf1972.22.4_96.

Okyay, T.O., Nguyen, H.N., Castro, S.L., Rodrigues, D.F., 2016. CO2 sequestration by ureolytic microbial consortia through microbially-induced calcite precipitation. Sci. Total Environ. 572, 671–680. http://dx.doi.org/10.1016/j.scitotenv.2016.06.199.

Sang, G., Lunn, R.J., El Mountassir, G., Minto, J.M., 2023. Meter-scale MICP improvement of medium graded very gravelly sands: Lab measurement, transport modelling, mechanical and microstructural analysis. Eng. Geol. 324, 107275. http://dx.doi.org/10.1016/j.enggeo.2023.107275.

Sarkis, M., Abbas, M., Naillon, A., Emeriault, F., Geindreau, C., Esnault-Filet, A., 2022. D.E.M. modeling of biocemented sand: Influence of the cohesive contact surface area distribution and the percentage of cohesive contacts. Comput. Geotech. 149, 104860. http://dx.doi.org/10.1016/j.compgeo.2022.104860.

Sarkis, M., Naillon, A., Emeriault, F., Geindreau, C., 2024. Tensile strength measurement of the calcite bond between bio-cemented sand grains. Acta Geotech. 19, 1555–1570. http://dx.doi.org/10.1007/s11440-023-02016-x.

Sarkis, M., Naillon, A., Emeriault, F., Geindreau, C., 2025. Shear strength measurement of a calcite bond between bio-cemented sand grains. Granul. Matter 27, 101. http://dx.doi.org/10.1007/s10035-025-01567-y.

Shen, Z., Jiang, M., Thornton, C., 2016. DEM simulation of bonded granular material. Part I: Contact model and application to cemented sand. Comput. Geotech. 75, 192–209. http://dx.doi.org/10.1016/j.compgeo.2016.02.007.

van Paassen, L.A., Ghose, R., van der Linden, T.J.M., van der Star, W.R.L., van Loosdrecht, M.C.M., 2010. Quantifying biomediated ground improvement by Ureolysis: large-scale biogrout experiment. J. Geotech. Geoenvironmental Eng. 136, 1721–1728. http://dx.doi.org/10.1061/(ASCE)GT.1943-5606.0000382.

Wang, Y., Soga, K., Dejong, J.T., Kabla, A.J., 2019. A microfluidic chip and its use in characterising the particle-scale behaviour of microbial-induced calcium carbonate precipitation (MICP). Géotechnique 69, 1086–1094. http://dx.doi.org/10.1680/jgeot.18.P.031.

Wang, H., Sun, X., Miao, L., Zhang, J., Yin, W., Wu, L., 2024. Sand and dust storms control for sustainable anti-desertification: Large-scale EICP-PVAc treatment field demonstration and insights. Acta Geotech. 1–19. http://dx.doi.org/10.1007/s11440-024-02494-7.

Wang, Y., Wang, Y., Konstantinou, C., 2023. Strength behavior of temperature-dependent MICP-treated soil. J. Geotech. Geoenvironmental Eng. 149, 04023116. http://dx.doi.org/10.1061/JGGEFK.GTENG-11526.

Whiffin, V.S., van Paassen, L.A., Harkes, M.P., 2007. Microbial carbonate precipitation as a soil improvement technique. Geomicrobiol. J. 24, 417–423. http://dx.doi.org/10.1080/01490450701436505.

Wu, H., Guo, N., Zhao, J., 2018a. Multiscale modeling and analysis of compaction bands in high-porosity sandstones. Acta Geotech. 13, 575–599. http://dx.doi.org/10.1007/s11440-017-0560-2.

Wu, H., Wu, W., Liang, W., Dai, F., Liu, H., Xiao, Y., 2023. 3D DEM modeling of biocemented sand with fines as cementing agents. Int. J. Numer. Anal. Methods Geomech. 47, 212–240. http://dx.doi.org/10.1002/nag.3466.

Wu, H., Zhao, J., Guo, N., 2018b. Multiscale insights into borehole instabilities in High-Porosity Sandstones. J. Geophys. Res.: Solid Earth 123, 3450–3473. http://dx.doi.org/10.1029/2017JB015366.

Wu, H., Zhao, J., Liang, W., 2020a. Pattern transitions of localized deformation in high-porosity sandstones: Insights from multiscale analysis. Comput. Geotech. 126, 103733. http://dx.doi.org/10.1016/j.compgeo.2020.103733.

Wu, H., Zhao, J., Liang, W., 2020b. The signature of deformation bands in porous sandstones. Rock Mech. Rock Eng. 53, 3133–3147. http://dx.doi.org/10.1007/s00603-020-02100-8.

Xiao, Y., He, X., Wu, W., Stuedlein, A.W., Evans, T.M., Chu, J., Liu, H., van Paassen, L.A., Wu, H., 2021a. Kinetic biomineralization through microfluidic chip tests. Acta Geotech. 16, 3229–3237. http://dx.doi.org/10.1007/s11440-021-01205-w.

Xiao, Y., He, X., Zaman, M., Ma, G., Zhao, C., 2022a. Review of strength improvements of biocemented soils. Int. J. Geomech. 22, 03122001. http://dx.doi.org/10.1061/(ASCE)GM.1943-5622.0002565.

Xiao, Y., Ma, G., Wu, H., Lu, H., Zaman, M., 2022b. Rainfall-induced erosion of biocemented graded slopes. Int. J. Geomech. 22, 04021256. http://dx.doi.org/10.1061/(ASCE)GM.1943-5622.0002239.

Xiao, Y., Stuedlein, A.W., Ran, J., Evans, T.M., Cheng, L., Liu, H., van Paassen, L.A., Chu, J., 2019. Effect of particle shape on strength and stiffness of biocemented glass beads. J. Geotech. Geoenvironmental Eng. 145, 06019016. http://dx.doi.org/10.1061/(ASCE)GT.1943-5606.0002165.

Xiao, Y., Wang, Y., Wang, S., Evans, T.M., Stuedlein, A.W., Chu, J., Zhao, C., Wu, H., Liu, H., 2021b. Homogeneity and mechanical behaviors of sands improved by a temperature-controlled one-phase MICP method. Acta Geotech. 16, 1417–1427. http://dx.doi.org/10.1007/s11440-020-01122-4.

Xiao, Y., Xiao, W., Wu, H., Liu, Y., Liu, H., 2023. Fracture of interparticle MICP bonds under compression. Int. J. Geomech. 23, 04022316. http://dx.doi.org/10.1061/IJGNAI.GMENG-8282.

Xiao, Y., Xiao, W., Wu, H., Zaman, M., 2024a. Tensile strengths and size effects of biocemented sands. Int. J. Geomech. 24, 06024004. http://dx.doi.org/10.1061/IJGNAI.GMENG-9353.

Xiao, Y., Yan, J., Wu, H., Zaman, M., 2024b. Tensile strength and fracture of interparticle MICP bonds. Int. J. Geomech. 24, 06024019. http://dx.doi.org/10.1061/IJGNAI.GMENG-10233.

Xiao, Y., Yan, J., Wu, H.R., Zaman, M., 2026. Shear fracture of MICP bonds considering particle shape. Int. J. Geomech. 26, 06026002. http://dx.doi.org/10.1061/IJGNAI.GMENG-13279.

Xiao, Y., Zhao, C., Sun, Y., Wang, S., Wu, H., Chen, H., Liu, H., 2021c. Compression behavior of MICP-treated sand with various gradations. Acta Geotech. 16, 1391–1400. http://dx.doi.org/10.1007/s11440-020-01116-2.

Yang, Y., Chu, J., Liu, H., Cheng, L., 2023. Improvement of uniformity of biocemented sand column using CH3cooh-buffered one-phase-low-pH injection method. Acta Geotech. 18, 413–428. http://dx.doi.org/10.1007/s11440-022-01576-8.

Yang, P., Kavazanjian, E., Neithalath, N., 2025. Discrete element simulations to predict the response of bio-cemented sands. Biogeotechnics 3, 100119. http://dx.doi.org/10.1016/j.bgtech.2024.100119.

Zhang, A., Dieudonné, A.C., 2023. Effects of carbonate distribution pattern on the mechanical behaviour of bio-cemented sands: A DEM study. Comput. Geotech. 154, 105152. http://dx.doi.org/10.1016/j.compgeo.2022.105152.

Zhao, Q., Li, L., Li, C., Li, M., Amini, F., Zhang, H., 2014a. Factors affecting improvement of engineering properties of MICP-treated soil catalyzed by bacteria and urease. J. Mater. Civ. Eng. 26, 04014094. http://dx.doi.org/10.1061/(ASCE)MT.1943-5533.0001013.

Zhao, Q., Li, L., Li, C., Zhang, H., Amini, F., 2014b. A full contact flexible mold for preparing samples based on Microbial-Induced calcite precipitation technology. Geotech. Test. J. 37, 917–921. http://dx.doi.org/10.1520/GTJ20130090.

Zhao, C., Xiao, Y., Chu, J., Hu, R., Liu, H., He, X., Liu, Y., Jiang, X., 2023. Microfluidic experiments of biological CaCO3 precipitation in transverse mixing reactive environments. Acta Geotech. 18, 5299–5318. http://dx.doi.org/10.1007/s11440-023-01938-w.

Zhao, H., Zhou, A., Shen, S.L., Arulrajah, A., 2025. A bottom-up hierarchical model for MICP-treated soil based on DEM. Comput. Geotech. 185, 107345. http://dx.doi.org/10.1016/j.compgeo.2025.107345.

Zheng, J., Lai, H., Cui, M., Ding, X., Weng, Y., Zhang, J., 2023. Bio-grouting technologies for enhancing uniformity of biocementation: A review. Biogeotechnics 1, 100033. http://dx.doi.org/10.1016/j.bgtech.2023.100033.

Zhu, Y.Q., Li, Y.J., Sun, X.Y., Guo, Z., Rui, S.J., Zheng, D.Q., 2025. A one-phase injection method to improve the strength and uniformity in MICP with polycarboxylic acid added. Acta Geotech. 20, 2279–2291. http://dx.doi.org/10.1007/s11440-024-02501-x.